AIP | Review of Scientific Instruments

Electron cyclotron emission measurements on JET: Michelson interferometer, new absolute calibration, and determination of electron temperature

S. Schmuck, J. Fessey, T. Gerbaud, B. Alper, M. N. A. Beurskens et al.

Citation: Rev. Sci. Instrum. **83**, 125101 (2012); doi: 10.1063/1.4768246
View online: http://dx.doi.org/10.1063/1.4768246
View Table of Contents: http://rsi.aip.org/resource/1/RSINAK/v83/i12
Published by the American Institute of Physics.

Electron cyclotron emission measurements on JET: Michelson interferometer, new absolute calibration, and determination of electron temperature

S. Schmuck,[1,a)] J. Fessey,[2] T. Gerbaud,[3] B. Alper,[2] M. N. A. Beurskens,[2] E. de la Luna,[4] A. Sirinelli,[2] M. Zerbini,[5] and JET-EFDA Contributors[b)]

JET-EFDA, Culham Science Centre, Abingdon, OX14 3DB, United Kingdom
[1]*Max-Planck-Institut fuer Plasmaphysik, Teilinsitut Greifswald, EURATOM-Assoziation, D-17491 Greifswald, Germany*
[2]*Euratom/CCFE Fusion Association, Culham Science Centre, Abingdon, Oxon. OX14 3DB, United Kingdom*
[3]*FOM Institute for Plasma Physics Rijnhuizen, Association EURATOM-FOM, Trilateral Euregio Cluster, The Netherlands*
[4]*Laboratorio Nacional de Fusion, Asociacion EURATOM-CIEMAT, Madrid, Spain*
[5]*Associazione Euratom-ENEA sulla Fusione, C.R. ENEA-Frascati, Via E. Fermi 45, 00044 Frascati, Roma, Italy*

(Received 14 September 2012; accepted 28 October 2012; published online 5 December 2012)

At the fusion experiment JET, a Michelson interferometer is used to measure the spectrum of the electron cyclotron emission in the spectral range 70–500 GHz. The interferometer is absolutely calibrated using the hot/cold technique and, in consequence, the spatial profile of the plasma electron temperature is determined from the measurements. The current state of the interferometer hardware, the calibration setup, and the analysis technique for calibration and plasma operation are described. A new, full-system, absolute calibration employing continuous data acquisition has been performed recently and the calibration method and results are presented. The noise level in the measurement is very low and as a result the electron cyclotron emission spectrum and thus the spatial profile of the electron temperature are determined to within ±5% and in the most relevant region to within ±2%. The new calibration shows that the absolute response of the system has decreased by about 15% compared to that measured previously and possible reasons for this change are presented. Temperature profiles measured with the Michelson interferometer are compared with profiles measured independently using Thomson scattering diagnostics, which have also been recently refurbished and recalibrated, and agreement within experimental uncertainties is obtained. [http://dx.doi.org/10.1063/1.4768246]

I. INTRODUCTION

A Michelson interferometer (MI) diagnostic is capable of measuring broadband intensity spectra in the microwave and near infrared spectral range.[1] Therefore, the Michelson interferometer is dedicated to probe the full electron cyclotron emission (ECE) spectrum emitted by high-temperature plasmas in fusion experiments with magnetic confinement.[2–4] At the JET tokamak, the Michelson interferometer, designed and built in the early 1980s,[5–7] operates to the present day as the corner stone of the ECE diagnostic system. Justified by its absolute calibration using the hot/cold technique the interferometer delivers information about the electron temperature T_e independent of the Thomson scattering (TS) diagnostics.[8–10] The JET plasma is probed from the low magnetic field side, and the vacuum line of sight is perpendicular to the magnetic field. Most JET plasmas have a high optical thickness,[11] i.e., above 3, for the second harmonic range in extraordinary mode (X2) polarization, which is therefore used to extract information about T_e. The Michelson interferometer with low spectral ($\Delta f = 3.66$ GHz) and temporal resolution ($\Delta t \approx 17$ ms) is complemented by a heterodyne radiometer ($\Delta f = 0.25$ GHz, $\Delta t \geq 5$ μs).[12] The radiometer probes the ECE subspectrum in ordinary (O) and extraordinary (X) mode polarization for the magnetic field range 1.7–4 T. This flexibility requires the cross-calibration against the Michelson interferometer for each pulse.[13] In some cases, the pedestal region of T_e can be probed on the in- and outboard sides simultaneously.[14] Hence, the necessity of the Michelson interferometer for the ECE diagnostic system at JET becomes clear: it is the basis for the independent determination of the absolute value of the electron temperatures by all the JET ECE diagnostics. In addition, the diagnostic is highly reliable because of its basic design and, if necessary, it can be maintained during plasma operation.

In addition to the standard application for the measurement of the T_e profile other diagnostic applications are possible. Since different harmonics have an individual dependence on plasma parameters and the line of sight, the Michelson interferometer can reveal information about the magnetic field, wall properties of the vacuum vessel, and the electron distribution function f_e parameterized to first order by T_e and the electron density n_e. For example, choosing an oblique line of sight, electrons are probed which are located in different regions of the velocity phase space, and thus non-Maxwellian features can be studied. At JET such a diagnostic is installed and was recently

a)Stefan.Schmuck@ccfe.ac.uk.
b)See the Appendix of F. Romanelli *et al.*, Proceedings of the 23rd IAEA Fusion Energy Conference 2010, Daejeon, Korea.

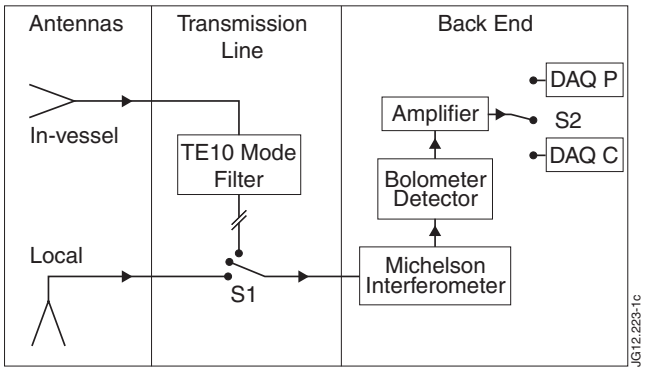

FIG. 1. Scheme of Michelson interferometer diagnostic at JET with major segments: antennas, transmission line, and back end. For the in-vessel antenna, the transmission line (∼40 m) includes a TE10 mode filter. Via the switch S1 the source in front of the in-vessel antenna or the local antenna with short transmission line (∼0.8 m) located in the diagnostic hall is chosen. The transmission line ends at the input port of the back end which comprises the Michelson interferometer unit, the bolometer detector, the amplifier stage, and the data acquisition (daq) system. For plasma (P) and calibration (C) operation, the daq system is chosen with switch S2.

independently calibrated.[15,16] Furthermore, the diagnostic potential allows the extraction of information about n_e from the optically thin part of the ECE spectrum, i.e., the broad spectral range for the 3rd and/or higher harmonics. The proof of principle[17] relies on ECE-tracing codes such as SPECE[18] and the Minerva Bayesian inference framework.[19] However, the reliability of the wider diagnostic application, including the testing of the plasma and wall model, depends strongly on the quality of the absolute calibration as does the determination of the T_e profile. A full system calibration was carried out in 2007. The measured system response was found to be different from that measured previously by about 25%.[20] Such a large change had not been measured before. Subsequent investigations indicate that the 2007 calibration suffered from several practical difficulties possibly including insufficient filling of the antenna pattern with the hot and cold sources mounted in the vacuum vessel. Therefore, a new full system calibration was carried out in 2010 and measures were taken to overcome the earlier difficulties.

Despite the long operation time of the interferometer the diagnostic has not been described in detail from hardware and data analysis point of view. Thus, this paper starts with the comprehensive description for the diagnostic design (Sec. II) including the segments for the antenna, transmission line, and interferometer back end. It presents the details of the 2010 absolute calibration and the hardware and the analysis technique employed (Secs. III and IV). Furthermore, the potential sources of systematic errors in the measurement are discussed and their possible magnitudes are estimated. Comparisons with T_e profiles measured with the refurbished Thomson scattering systems are included. Conclusions are drawn in Sec. V. For completeness, the general derivation of the calibration factors and their application to obtain the ECE spectrum for plasma operation are given in the Appendix.

II. DIAGNOSTIC DESIGN

The Michelson interferometer diagnostic at JET consists of three major segments: antennas, transmission line, and back end (see Fig. 1). The latter is located in the JET diagnostic hall. The in-vessel antenna is used with the associated transmission line for probing the plasma and absolute calibration. For measurements in the diagnostic hall, i.e., local measurements, for example, to characterize a source spectrally, the local antenna with short transmission line is employed. The main elements of the back end are the interferometer unit, the bolometer detector, the post-detection amplifier, and the data acquisition system. Detailed descriptions of the different parts of the diagnostic follow. These summarize the information in Refs. 5–7 and 21–29 and complete the diagnostic description by presenting additional facts.

A. Antennas and transmission line

The aperture of the in-vessel antenna is located at the major radius R = 4.126 m and height z = 0.353 m (see

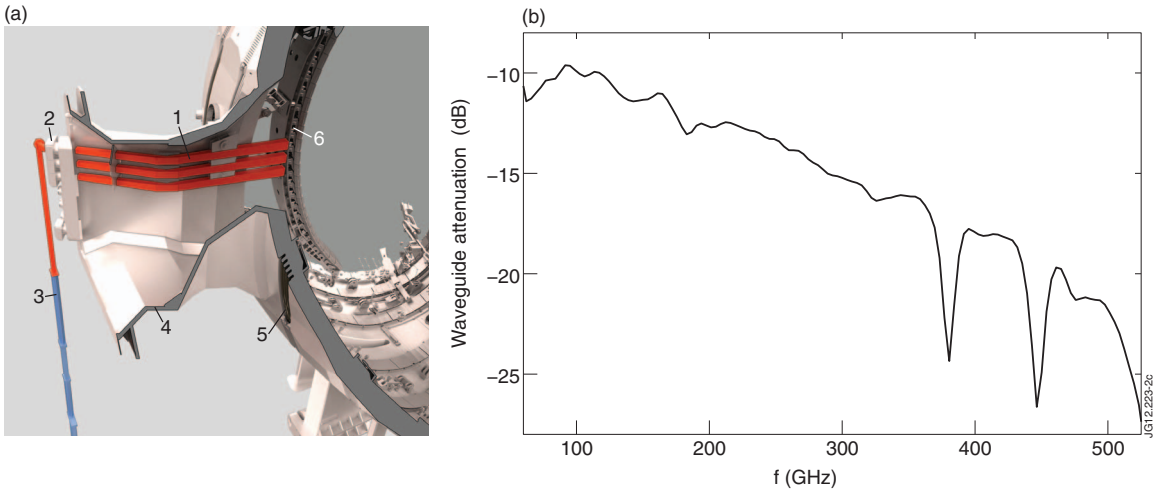

FIG. 2. (a) Diagnostic front end according to JET model.[30] (1) In-vessel antenna, (2) location of polarizer with horizontal wires, (3) transmission line (red) including TE10 mode filter (blue), (4) cross-section of diagnostic port in octant 7, (5) outer wall of JET vessel, (6) limiter structure at inner wall of JET. (b) Attenuation of transmission line for in-vessel antenna for spectral range 60–525 GHz. Around the frequencies 380.20 GHz and 440 GHz absorption by water vapour increases the attenuation.

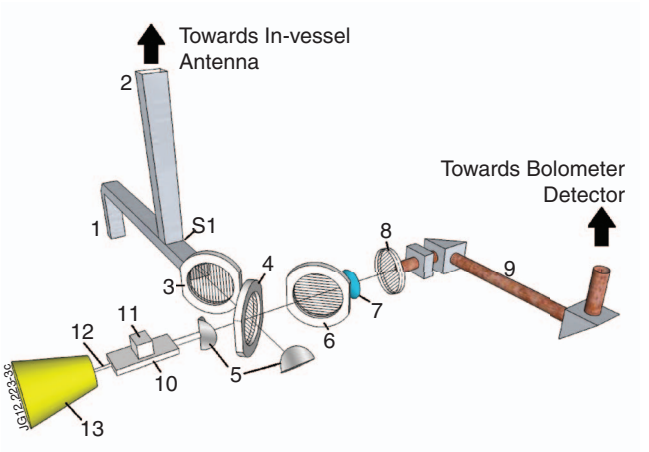

FIG. 3. Design of Michelson interferometer unit using switch S1 (see Fig. 1). (1) Local antenna with transmission line (0.8 m), (2) taper for transmission line of in-vessel antenna, (3) vertical polarizer, (4) beam splitter, (5) roof top mirrors, (6) horizontal polarizer, (7) TPX lens, (8) grid attenuator (in place for plasma operation), (9) circular waveguide, (10) mirror translator (air-bearing) with micrometer scale on top, (11) scanning head, (12) silver steel rod, (13) linear shaker.

component 1 in Fig. 2(a)) in octant 7 of the JET torus. The horizontal line of sight is at 3.5° with respect to the radial direction. The antenna with the length of 1.6 m incorporates in the middle one mitre bend at 30° and is manufactured from Inconel. The rectangular antenna cross-section decreases from 50 mm × 65 mm at the plasma end to 40 mm × 30 mm at the inner JET wall. For the TE10 mode, the antenna pattern is characterized theoretically and experimentally by the acceptance angle of about ±3° in the spectral range 100–130 GHz.[21,22]

The antenna ends at the double window with diameter 68 mm. The window is secured with a high temperature vacuum seal and is made from two wedged disks of Z-cut crystal quartz. Outside the vessel the transmission line is about 40 m long, which is filled entirely with air including water vapour, and comprises 12 mitre bends (4 in E plane, 8 in H plane) ending at the back end in the diagnostic hall. The attenuation of the transmission line as determined in 2010 drops from −10 dB at 100 GHz to −21 dB at 500 GHz (see Fig. 2(b)). Immediately after the vacuum window the horizontal waveguide with cross-section 40 mm × 30 mm carries the grid with horizontal wires to transmit waves in X-mode polarization (see component 2 in Fig. 2(a)). Close to the polarizer the waveguide falls vertically after the first two mitre bends and is connected to the TE10 mode filter[22] with the length of 2 m shown by component 3 in Fig. 2(a). From the filter output onwards the S band waveguide (72 mm × 34 mm) is used in tall mode, meaning that the E field vector of the wave is parallel to the long side of the waveguide, up to the diagnostic hall. Close to the inner wall of the torus hall the transmission line has an air gap of 1 cm in length to insulate the waveguide electrically from the JET vessel. In the diagnostic hall, the waveguide tapers to the rectangular cross-section 40 mm × 30 mm along a length of 1.20 m (see component 2 in Fig. 3). The last bend connects the vertical waveguide with the horizontal input port of the interferometer. A removable aluminium plate constitutes the last bend, and so when this switch (S1 in Figs. 1 and 3) is removed the horizontal part of the antenna is connected to the interferometer input port. This antenna is a waveguide of 0.8 m in length with cross-section 40 mm × 30 mm. The antenna aperture points downwards via a mitre bend 15 cm before the end.

B. Michelson interferometer

The Martin-Puplett interferometer (see Fig. 3) is sensitive to the difference in the source spectra held by its two input ports. Thereby, just one of the output ports is used for signal detection. The interferometer uses wire grids with the wire diameter 10 μm and spacing 25 μm. The first input port holds the permanent source made from ECCOSORB AN-72[31] at ambient temperature. The second one holds the rectangular waveguide connected to the in-vessel or the local antenna. Behind the first grid the vertical and horizontal electric field carries the information of the permanent source and the one to be probed, i.e., the plasma or any locally placed source, respectively. The beam splitter transmits and reflects the same fraction for both polarizations. Therefore, its wires rising with the angle 33° appear at 45° when the filter is rotated by 45° with respect to its central vertical axis. Each partial beam enters a separate arm holding a roof top mirror with aperture angle of 90°. By the double reflection at the mirror, the beam polarization direction flips by 90°. Hence, each returning beam is affected in the opposite way by the splitter resulting in the reunification of the partial beams. After passing the last grid with horizontal wire orientation a lens made from polymethylpentene (TPX)[32] with focal length of 15 cm is used. The beam is focused into the aperture of the circular waveguide with diameter 25 mm and length 0.5 m. The circular waveguide ends at the entrance window of the cryogenic vessel holding the bolometer detector. During plasma operation an attenuating grid is inserted between the lens and the circular waveguide. As a consequence, the power incident on the detector reduces by approximately 5 dB, and the range for the linear detector response is extended. The grid with diagonal wire direction is placed almost perpendicular to the optical axis.

In the interferometer arms, the change in the optical path difference between the partial beams is achieved by the direct movement of one roof top mirror. The mirror translator is connected to the shaker by a thin silver steel rod (see components 10, 12 and 13 in Fig. 3) with 1 mm in diameter at the ends tapering to 250 μm in the middle section and 30 mm in length. The rod is introduced to break if the stress on the moving parts is increasing. The shaker oscillates at a frequency of 30 Hz. Its peak-to-peak amplitude is about 16.3 mm covering mainly the single-sided interferogram region. The corresponding maximum optical path difference achieved is about 27 mm.

The air-bearing stage (not shown) ensures the linear movement of the gliding mirror translator and reduces friction.

C. Bolometer detector and amplifier

The semiconductor indium antimonide bolometer detector[25,26] is designed to operate at the ambient temperature

of liquid helium (4.2 K). Therefore, the back of the detector is attached to a reservoir of liquid helium (6.5 l) in the centre of a cylindrical cryogenic vessel[25] (not shown). In addition, a vacuum chamber and a reservoir with liquid nitrogen (6.5 l) surround the vessel centre for insulation from the laboratory environment.

The radiation leaving the circular waveguide (see Sec. II B) passes through a window embedded in the cryogenic vessel. Inside the vessel, the Winston cone[33] with aperture diameter 26 mm concentrates the radiation along 42 mm to its exit with diameter 6.5 mm where the bolometer detector is located. At the window, Fluorogold foil is placed to limit the spectral range to about 1.0 THz[26] which can enter the vessel.

At 4.2 K the detector absorbs incident photons which increases the conductivity (hot electron effect). The corresponding voltage change across the detector, i.e., the output voltage, is measured. For operation a bias current needs to be applied to the detector, the magnitude of which affects the detector sensitivity. To minimize electrical noise, the bias current of about 60 μA is provided by rechargeable long-life batteries (10 V) via a high resistance ($\approx$164 kΩ) acting as a constant current source. The detector sensitivity provided by the supplier exceeds 500 V/W and 1000 V/W for the spectral ranges 60–1000 GHz and 100–250 GHz, respectively. The detector has a recovery time of 1 μs and the noise-equivalent power of 2×10^{-12} W/Hz$^{0.5}$ for the first amplifier stage with bandwidth 600 kHz and fixed amplification of 40 dB ($\times$100). For the second stage, the bandwidth is set to 30 kHz realized by a first order resistor-capacitor filter, and the amplification used is 14 dB and 50 dB for plasma and calibration operation, respectively. For radiation up to 1 THz, which marks the cutoff frequency of the Fluorogold foil, the Fourier components of the detector signal are all below 10 kHz. This value is sufficiently exceeded by the chosen cutoff frequency (30 kHz) of the second amplifier ensuring that the induced phase shift is insignificant. The linearity of the detector response including the amplifier stage has been confirmed.[23]

The rapid reciprocating motion of the roof-top mirror can induce vibrations in the interferometer supporting structure and these, in turn, can produce vibrations of the detector. Since the detector is microphonic at a low level, mechanical decoupling of the interferometer unit and the detector is necessary. This is achieved by using separate metal frames.

D. Data acquisition

The acquisition of the detector output voltage (see Sec. II C) synchronized with the optical path difference (see Sec. II B) is essential for achieving an accurate spectrum by processing the interferogram data. Since the mirror position and thus the optical path difference change sinusoidally with time, the sampling at a fixed frequency deforms the acquired interferogram. Therefore, an incremental linear encoder[34] is used to sample the interferogram equidistantly in the spatial domain. On top of the mirror translator, a micrometer scale with an additional reference marker is fixed and probed by a scanning head (see components 10 and 11 in Fig. 3). The encoder electronics generates individual transistor-transistor logic (TTL) signals, when the reference marker passes the optical head, which happens once per interferogram scan, and the direction of the mirror motion changes at the turning points. Furthermore, a TTL signal is available which encodes the spatial position of the mirror. The latter are used to trigger the data acquisition for the detector output voltage when the mirror moves by 10, 20, 40 or 80 μm depending on the chosen setting.

Historically, the data acquisition (daq) systems differ for plasma and calibration operation. For the former, the spatial increment 80 μm is used corresponding to the average and maximum sampling frequency of about 11 kHz and 17 kHz, respectively. The analog-to-digital converter (ADC) with 12 bit resolution used since the 1980s covers the dynamical range of 10 V and has limited memory storage for 2^{16} data words. For the spatial increment 80 μm, giving about 200 data words per interferogram, the memory fills up in 5.5 s. Therefore, most interferograms must be omitted during a JET pulse with 30 s duration which is handled by the diagnostic control program.

For calibration operation, the situation changes completely. Since broadband sources are used with temperatures below 1000 K, the signal-to-noise ratio (SNR) is low and the main interferogram located around the zero-path difference position is narrow. Hence, the interferogram is sampled with the spatial increment 20 μm determining the sampling frequency with the average and maximum value of about 44 kHz and 70 kHz, respectively. The SNR is increased by averaging individual interferograms coherently. Before 2010 diverse daq systems averaged the output voltage of the detector in real-time for several minutes coherently. Thereby, the information about individual interferograms was lost and numerical instabilities could arise. On the contrary, the daq system applied for the calibration in 2010 stores all raw data to hard disc enabling post-measurement treatment. Thereby, the daq card[35] used has 16 bit ADC resolution and covers the dynamical range $\pm$10.5 V. Due to the permanent storage, individual interferograms, which are corrupted by spikes possibly picked up from radio or mobile emission (see Fig. 5(a)), can be identified and removed. Besides the detector output voltage, the TTL signal for the reference marker is acquired to check and therefore guarantee the coherent averaging procedure. To reduce the physical hard disc memory, the ADC level is stored in binary format. The conversion to voltages is achieved using the coefficients for the fourth order polynomial specific for the daq card. Removing faulty interferograms, checking the interferogram coherence and converting the unitless raw data to voltage for a data file with 250 MB, corresponding to measurements for 20 min, takes less than 30 s with the averaging software developed. For each data file, the analysis results in two averaged interferograms one each for the forward and backward direction of the mirror motion. In addition, for each mirror position the standard deviation is stored. This feature allows the identification of the interferogram region which is averaged coherently.

Recently, a conversion factor was found between the daq systems used for plasma and calibration (2010) operation. Local and plasma measurements show that the daq system for plasma operation gives a signal which is reduced by about

2%. Probably, this conversion factor is present since the construction of the interferometer, and it is nowhere corrected.

Since the daq system used during the calibration session in 2010 has proven its reliability it is used now for plasma operation from JET pulse 83 144. Besides removing the conversion factor the temporal resolution (~60 Hz) of the diagnostic limited by the shaker frequency (see Sec. II B) is achieved.

E. Diagnostic protection

The diagnostic design includes several aspects for protecting the diagnostic hardware. In general, a detected malfunction results in the interlock of the power supply for the shaker stopping the mirror movement which happens once a month or less. Causes for interlocking are the changing shaker characteristic, the breaking of the connector between shaker and mirror translator, and the drop in air flow to the air bearing.

The shaker characteristic changes after several hours of running time, and thus the maximum amplitude and the centre of the sinusoidal movement for the mirror vary. To keep the movement in a well-defined range, the air bearing supporting the mirror translator has a limiting micro-switch at either side. The translator (see component 10 in Fig. 3) has small arms one on each side which can activate the micro-switch stopping the Michelson interferometer.

If the stress is increasing on the moving parts, the steel rod (see component 12 in Fig. 3) breaks causing the activation of the micro-switches.

In case the pressure in the air bearing system falls below a threshold, which is set manually by an air pressure switch, the electronics recognizes a malfunction.

F. Maintenance

During plasma operation little effort is needed for the diagnostic maintenance. The cryogenic vessel (see Sec. II C) is refilled with liquid helium in 20 min with two persons once every two weeks. The Michelson has been equipped with an automatic liquid nitrogen (LN2) refilling system. The system operates between set points using a probe for the LN2 level and a meter system and takes around 15 min to refill the system from 30% to 80%. The 250 l LN2 Dewar connected lasts for around 10 days.

Since 2011 the bias voltage for the detector (see Sec. II C) is monitored on a daily/weekly basis. When the voltage drops to the 9 V level the batteries are recharged for 12 hours during non-plasma operation time.

The adaptation of the rod length, i.e., the distance between shaker and mirror extension, and/or the replacement takes 10 min and happens every some ten hours of running time for the shaker. The replacement of the shaker after the running time of about 200 hours takes approximately 60 min.

The main maintenance work is demanded by the preparation and execution of the absolute calibration which is described separately in Chaps. 3 and 4 for the session in 2010. The absolute calibration is complemented by the relative calibration using JET pulses for which the magnetic field ramps down from 3.5 T to 1.7 T.[36] The JET operation limits mean that at least two pulses are needed to perform the full ramp. These ramp pulses are carried out about once a year.

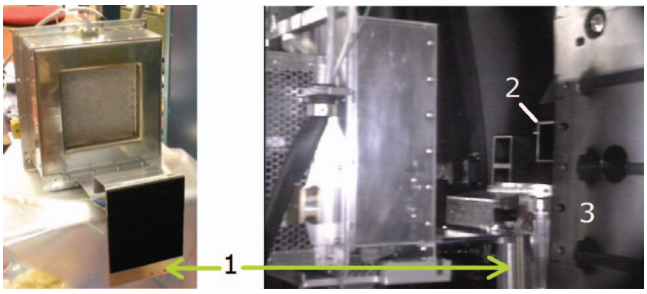

FIG. 4. (Left) Front view of cold- and hot-source. The cold-source realized by the microwave absorber material TK[38] sits on the aluminium switch (1) moving up- and downwards. The active surface (black) of the TK material covers 17 cm × 20 cm. The hot-source is located behind the cold-source having the active surface (grey) with area 20 cm × 20 cm. An aluminium plate connects both sources. (Right) Side view of cold- and hot-source placed in front of in-vessel antenna (2). The position of the switch (1) is down, thus the diagnostic antenna, partly hidden by the limiter (3, also see component 6 in Fig. 2(a)), faces the hot-source. The diagnostic line of sight crosses almost the centre of each source (top view not shown). The distance from the active surface of the hot-source to the antenna is less than 33 cm.

III. CALIBRATION SETUP

The absolute calibration of the Michelson interferometer at JET utilizes the hot/cold technique. The calibration sources are integrated in the stand-alone setup which is remotely controlled via the network. Due to JET radiation protection regulations the placement of the mounting structure together with both sources needs to be carried out by the remote handling system MASCOT.[37] Once the deployment is completed, the calibration setup requires no additional auxiliary resources. The continuous operation of the setup was achieved without malfunction for several days. Details about the stand-alone setup are described below.

A. Cold-source

Typically for absolute emission measurements in the microwave range the cold-source is realized by a microwave absorber material at the temperature of LN2 (77 K). However, because of safety considerations, the use of cryogenic fluids at JET is limited and so a material at ambient temperature with black body properties needs to be used for in-vessel calibration. The microwave absorber material TK, which has black body properties from at least 100 GHz upwards,[38] meets the regulations for contamination hazards of the JET vessel and is therefore used. Individual TK tiles form the active surface with an area of about 17 cm × 20 cm. The cold-source is attached to an aluminium plate of equal dimension (see Fig. 4 left). Between the tiles and the plate a thermocouple is mounted to measure the temperature.

B. Hot-source

The hot-source is a remote device electronically heated (see Fig. 4 left). Its principal component is a copper plate, in which 12 cartridge heaters are inserted capable of heating the plate uniformly to the physical temperature of 873 K within about 40 min. The radiating surface is situated on top

of the copper plate with an area of 20 cm × 20 cm and has a moth-eye structure filled with a SiC grit suspended in an inorganic binder. The radiating plate is housed in an aluminium alloy box and insulated with a high temperature refractory board. The outer box has been designed specifically to aid remote handling by MASCOT within the JET torus. The control electronics are mounted on the rear of the outer box. The only connections are a 110 V power supply and an ethernet cable that connects the in-built web server to the local area network. Six mineral insulated thermocouples are embedded uniformly within the radiating screed. One central thermocouple is used to lock the plate temperature via the closed loop control of a proportional-integral-derivative controller.

C. Switching between sources

The periodical switching between the sources is achieved by the mechanical up/down movement of a vertical aluminium plate (see component 1 in Fig. 4) which carries the cold-source (see Sec. III A). A horizontal aluminium plate of length ∼30 cm connects the switch and the outer box surrounding the hot-source. Switching between the sources is applied every 20 or 30 min, and the process itself takes less than 30 s.

D. Mounting structure

The mounting structure is designed to guarantee reproducibility for the localization of the sources with respect to the in-vessel diagnostic antenna. The positioning is realized by a plug inserted into another antenna below the diagnostic antenna. The mounting structure carries the assemblage of the cold- and hot-source such that the diagnostic line of sight crosses the centre of both active surfaces (see Fig. 4 right). The distance from the antenna aperture to the cold- and hot-source is less than 5 cm and 33 cm, respectively. After placing the mounting structure and the sources with MASCOT within 3 hours, no resources are needed for support.

E. Overall control and monitoring program

During the absolute calibration the software developed with LabVIEW® controls the main parameters, automatizes all necessary steps and monitors the state of the setup. After reaching the requested physical temperature for the hot-source, the initial shutter position is set. The acquisition starts to take data for the time interval specified by the user, in doing so the durations 20 and 30 min have been used. When the time interval has elapsed, the data acquisition stops and the switch moves. Afterwards the data acquisition starts for having the complementary source in place. This hot/cold cycle is repeated automatically. At the same time, online monitoring of the main parameters, i.e., the current physical temperatures of both sources and the switch position, is available describing the calibration setup extensively. In addition, these parameters are stored on hard disc every 5 s. Throughout the calibration of four days the state of the stand-alone setup was always defined and sufficiently steady. In total, about 600 gigabytes of data for the interferogram and reference marker were continuously acquired.

IV. ANALYSIS TECHNIQUE

The absolute calibration of the Michelson interferometer at JET has been carried out since the 1980s by different diagnosticians each having their own approach. General information and specific details for each approach can be found in Refs. 39 and 40. In the following, the analysis technique of the calibration session in 2010 is described. The evaluation of the absolute calibration factors, and how they are used in the analysis during JET plasma operation, requires measured and/or derived quantities like the difference interferogram, recovered difference spectrum, difference input intensity, and the grid transmission. After the definition of the calibration factors is given the detailed description for the derivation of each relevant quantity follows. In addition, the corresponding uncertainty for the quantity at hand is evaluated for the spectral domain expressed by the standard error of the mean. Therefore, the uncertainties of the calibration factors can be captured by Gaussian error propagation. All results presented rely on measurements carried out in 2010 with the Michelson interferometer to be calibrated and the continuous daq system including the post-measurement digital averaging technique (see Sec. II D). Each measurement reflects the integration time of several hours, at least. The necessary switching between different sources is realized every 20 or 30 min.

A. Definition and application

A general derivation of the calibration factors including units can be found in the Appendix. For JET conditions, a grid attenuator with transmission T is inserted during plasma operation (see component 8 in Fig. 3). Therefore, the calibration factors C_f defined by Eq. (A5) need the modification

$$C_f = A_C^{-1} \frac{\mathrm{PC}\left(\mathrm{DFFT}^{-1}\left\{g\left(V^{Hot} - V^{Cold}\right)\right\}\right)}{\Delta I} T = \frac{\Delta S}{\Delta I} T, \tag{1}$$

where the ratio of the recovered difference spectrum ΔS to the difference input intensity ΔI enters. ΔS is evaluated using the post-detection amplification A_C, the phase correction method PC, the inverse discrete fast Fourier transformation routine DFFT^{-1}, the apodization function g and the difference interferogram $V^{Hot} - V^{Cold}$. During plasma operation the amplification A_P is reduced with respect to A_C by some orders of magnitude. The linearity of the diagnostic sensitivity necessary to apply C_f to processed data measured during plasma operation has been confirmed.[23] The calibrated spectrum, i.e., the ECE spectrum, is evaluated by

$$I_{\mathrm{ECE}} = A_P^{-1} \frac{\mathrm{PC}\left(\mathrm{DFFT}^{-1}\left\{g\left(V^{\mathrm{ECE}}\right)\right\}\right)}{C_f} = \frac{S^{\mathrm{ECE}}}{C_f} \tag{2}$$

from a measured interferogram V^{ECE} processed to give the recovered spectrum S^{ECE}. Thereby, the coherence between C_f and S^{ECE} is ensured by using the same implementation for PC, DFFT^{-1}, and g in Eqs. (1) and (2).

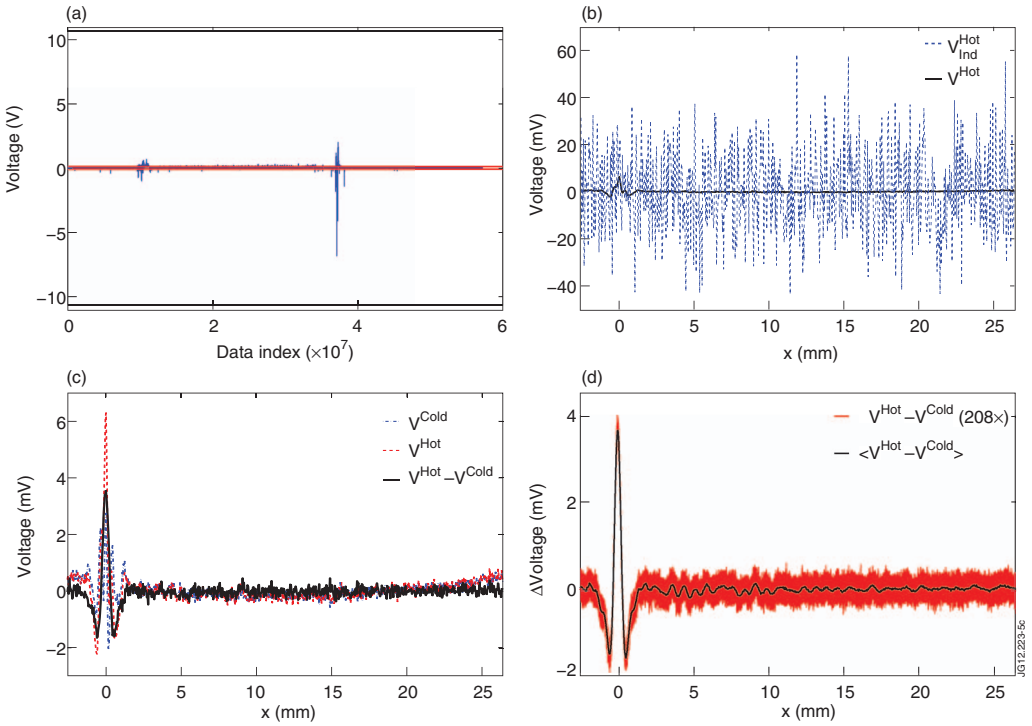

FIG. 5. Processing steps for derivation of difference interferogram $V^{Hot} - V^{Cold}$ from raw data taken during absolute calibration in 2010. (a) Raw data trace (blue). In 20 min of continuous data acquisition, almost 6×10^7 voltage values (~70 000 individual interferograms) are stored on hard disc permanently. Spurious signals can exceed the interferogram data by more than three orders of magnitude, for example, around data index 3.5×10^7. The post-measurement averaging method neglects individual interferograms which are outside the acceptance region ±100 mV (red). The ADC covers the dynamical range ±10.5 V (black). (b) Interferogram data V^{Hot} dependent on optical path difference x. Individual interferograms (blue) each acquired in 17 ms suffer from noise with standard deviation 17.5 mV. The averaged interferogram (black) is strongly asymmetric around the ZPD position ($x = 0$ mm). Digital averaging of a raw data trace acquired for 20 min increases the SNR from about 1:3 to about 60:1 around the ZPD position. (c) Digitally averaged interferograms V^{Cold} for cold-source (blue) and V^{Hot} for hot-source (red). The difference interferogram (black) removes the asymmetry around the ZPD position and the back ground voltage signal which is obvious for x>25 mm. (d) Two hundred eight difference interferograms $V^{Hot} - V^{Cold}$ (red) and overall average $\langle V^{Hot} - V^{Cold}\rangle$ (black). The latter reflects 8.6×10^6 individual interferograms and integration time of 3.4 days per source. The final SNR at $x = 0$ mm is about 430:1.

B. Difference interferogram

During calibration measurements the detector output voltage is amplified by the factor $A_C = 10^{4.5}$, stored permanently and averaged afterwards. Thereby, the stored raw data trace for 20 min (see Fig. 5(a)) consists of about 35×10^3 individual interferograms for each mirror direction. Occasionally, spurious signals in the range ±10 V perturb the measurements (see Fig. 5(a)). Since in the worst case a single spike of 10 V corrupts the measurements of 20 min, the averaging method rejects affected interferograms to ensure the data quality. Typically, at the zero-path difference (ZPD) position, at which all spectral components interfere constructively, the averaged interferogram has its maximum of about 6 mV (see Figs. 5(b) and 5(c)) when the hot-source is in place. At the same time the noise at a fixed optical path length is described by the standard deviation 17.5 mV (see Fig. 5(b)). Therefore, the SNR is about 1:3 at the ZPD position and is increased by averaging for the duration of 20 min to 60:1. Note, at nodes where the interferogram vanishes the SNR is decreased by several orders of magnitude. The average of each raw data trace, i.e., the average interferogram V^{Cold} or V^{Hot}, represents the continuous interferogram by 724 samples in the optical path difference range from −2.54 mm to 26.38 mm. The interferograms V^{Cold} and V^{Hot} remain slightly noisy, and the asymmetry around the ZPD position is obvious (see Fig. 5(c)). The latter feature reduces considerably for the difference interferogram $V^{Hot} - V^{Cold}$ (see Fig. 5(c)). In total, 208 difference interferograms are available corresponding to about 8.6×10^6 individual interferograms and 3.4 days of integration duration per source (see Fig. 5(d)). Thereby, subsequent interferograms V^{Cold} and V^{Hot} are used for the difference. The overall average for the difference interferogram $\langle V^{Hot} - V^{Cold}\rangle$ (see Fig. 5(d)) clearly shows structures for large optical path differences and a high degree of symmetry around the ZPD position. In addition, the reduction of the ratio of the noise level to the ADC resolution (0.325 mV) to 1:35 is achieved.

C. Recovered difference spectrum

The recovery of the difference spectrum ΔS from the difference interferogram $V^{Hot} - V^{Cold}$ uses standard techniques like apodization, zero-padding, discrete fast Fourier transformation, and phase correction.[41] The corresponding processing is given in Eq. (1). Thereby, the apodization window function g is a linear ramp in the double-sided region ($|x| \le 2.54$ mm) and the first quarter period of a cosine function bringing the single-sided region (2.54 mm$<x<$26.38 mm) smoothly to 0. Zero-padding above 26.38 mm increases the spectral resolution from 5.68 GHz to 3.66 GHz.

Processing $\langle V^{Hot} - V^{Cold}\rangle$ (see Fig. 5(d)) gives the smooth recovered difference spectrum (see Figs. 6(a)

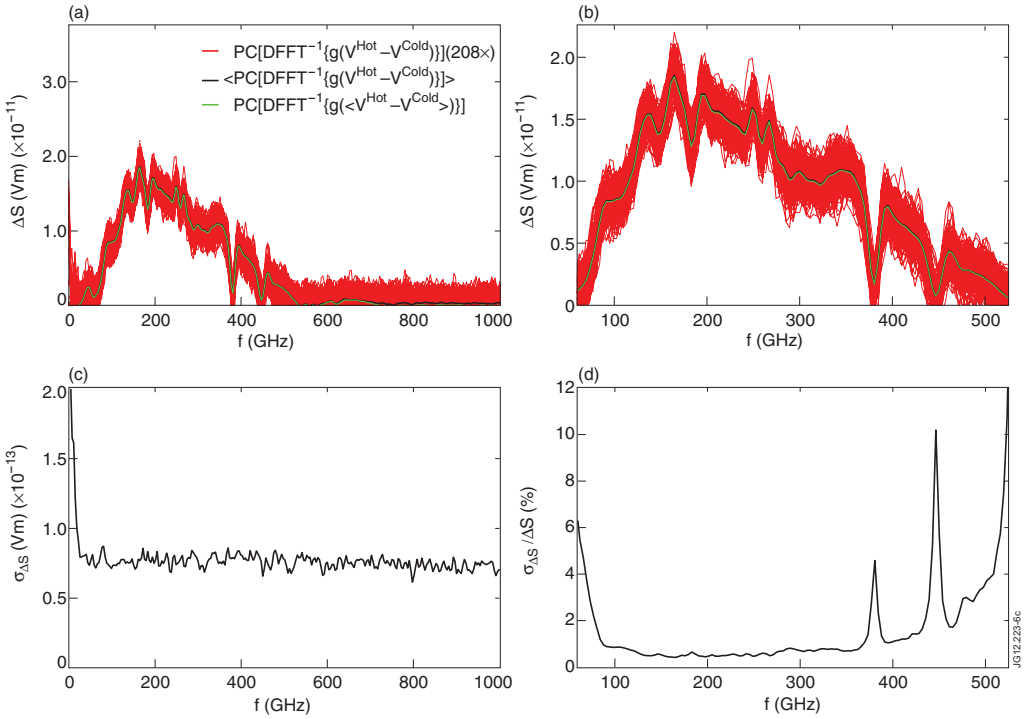

FIG. 6. Recovered difference spectra ΔS (first row) with uncertainty $\sigma_{\Delta S}$ and relative uncertainty $\sigma_{\Delta S}/\Delta S$ (second row). (a) Spectral range 0–1000 GHz. The average in the spectral domain (black) arises from 208 individuals (red) and agrees with the result for the overall difference interferogram (green) within 2% below 500 GHz. (b) Spectral range 60–525 GHz. The dips at 183.31 GHz, 380.20 GHz, and 440 GHz indicate water absorption lines. (c) $\sigma_{\Delta S}$. The uncertainties are almost constant on absolute scale for a broad spectral range (f>30 GHz). (d) $\sigma_{\Delta S}/\Delta S$. Clearly, the Michelson can be calibrated for the range 60–525 GHz. For the spectral range 100–350 GHz $\sigma_{\Delta S}/\Delta S$ falls below 1%. The water absorption lines at 380.20 GHz and around 440 GHz influence the relative accuracy far more than the one at 183.31 GHz.

and 6(b)). Non-vanishing components are present in the spectral range 30–525 GHz and 600–700 GHz, and the maximum is located around 200 GHz. The processing of the 208 individuals $V^{Hot} - V^{Cold}$ (see Fig. 5(d)) maps the uncertainties from the spatial to the spectral domain (see Figs. 6(a) and 6(b)). The averages for both approaches coincide below 500 GHz. The uncertainty $\sigma_{\Delta S}$ in the spectral domain remains almost constant above 30 GHz (see Fig. 6(c)) and, thus, is independent on the signal itself. Nevertheless, the relative uncertainty $\sigma_{\Delta S}/\Delta S$ varies with frequency (see Fig. 6(d)) and certifies the spectral range 50–500 GHz for calibration. Furthermore, inside the range 100–350 GHz the relative uncertainty remains below 1%. Two peaks at 380.2 GHz and 440 GHz indicate the influence of water vapour absorption lines resulting in high uncertainties at these frequencies. The determination is not affected by the water vapour absorption line at 183.31 GHz.

D. Difference input intensity

In order to derive the difference input intensity $\Delta I = I_f^{Hot} - I_f^{Cold}$, the spectrum of each source, i.e., I_f^{Cold} for the cold-source (see Sec. III B) and I_f^{Hot} for the hot-source (see Sec. III C), needs to be characterized. Thereby, the spectrum is parameterized by the radiative temperature using the Rayleigh-Jeans law ($I_f = (k_B/c^2)f^2 T_{Rad}$).

For the cold-source, realized by the microwave absorber material TK, the radiative temperature T_{Rad}^{Cold} equals the physical temperature T^{Cold}, which is measured by a thermocouple (Sec. III B) every 5 s during the absolute calibration. A periodical variation in T^{Cold} during the hot-/cold-source cycles is present. For example, T^{Cold} rises from about 307 K to 312 K in 20 min, when the TK material is placed between the in-vessel antenna and the hot-source, and drops accordingly, when removed. For the complete calibration session T^{Cold} averages to 309.8 K, and, in addition, the standard deviation σ_{TCold} reads 1.24 K.

The hot-source is characterized at the physical temperature 873 K by the hot/cold technique using the TK material at 77 K (LN2) and at 296 K (room temperature) as references. For the characterization each source is placed in front of the local antenna (see Sec. II A) at the distance less than 15 cm, which is assumed to be close enough to fill the antenna pattern sufficiently. The determined radiation temperature T_{Rad}^{Hot} is smaller by about 100 K with respect to its physical temperature in the spectral range 70–725 GHz (see Figs. 7(a) and 7(b)). Furthermore, T_{Rad}^{Hot} decays from 800 K to 760 K. The uncertainty σ_{THot} is less than 3 K/6 K for 150–350 GHz/100–500 GHz (see Fig. 7(c)). Since the corresponding relative uncertainty $\sigma_{THot}/T_{Rad}^{Hot}$ is less than 1% (see Fig. 7(d)), T_{Rad}^{Hot} is determined with high precision for a broad spectral range. However, since somewhere below 100 GHz the TK material loses its black body property, T_{Rad}^{Hot} suffers from a systematic error emphasised by the strong increase to 860 K around 60 GHz. Using the spectral characterizations described above, at the aperture of the in-vessel antenna the difference input intensity ΔI is present (see Figs. 7(e) and 7(f)). Due to the square law in frequency

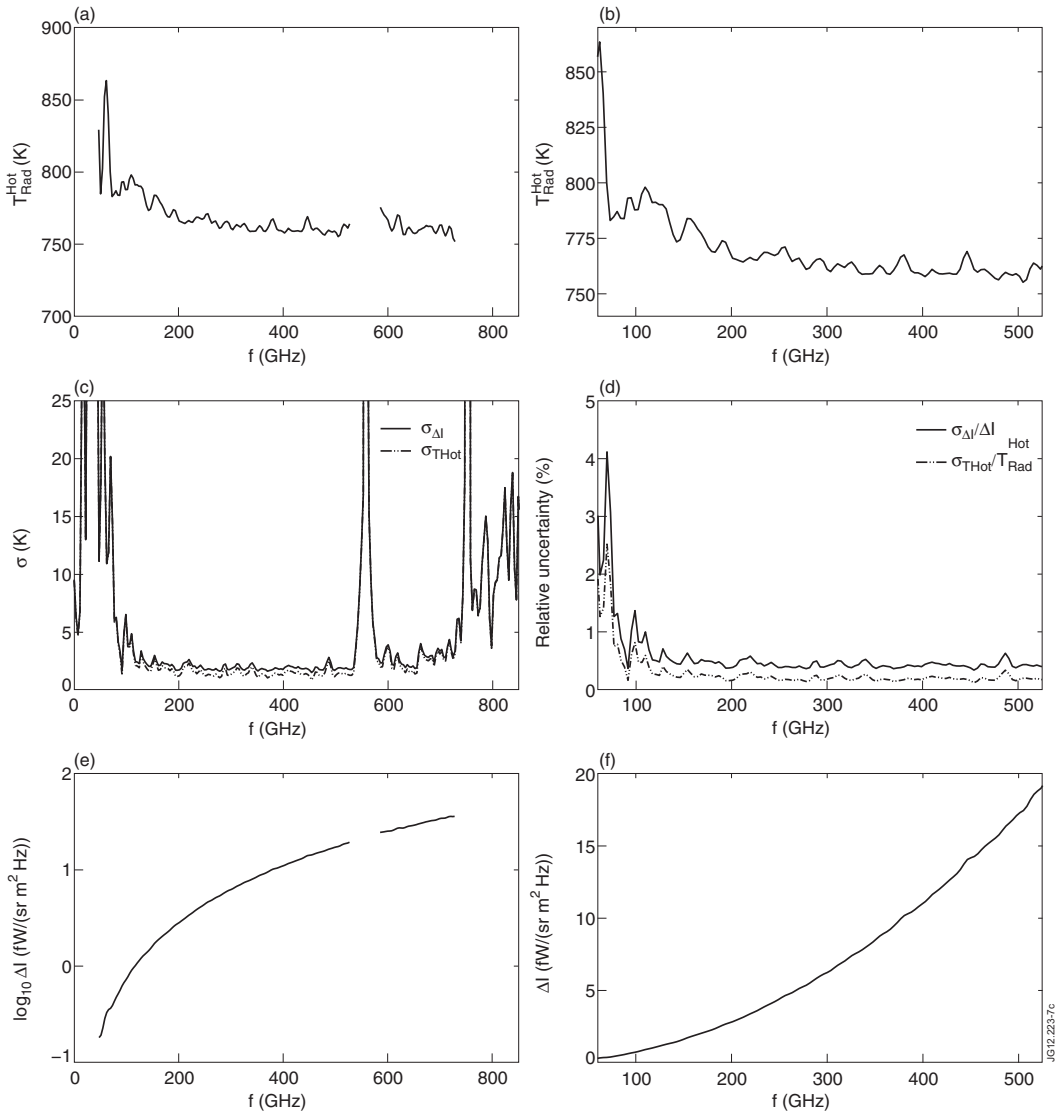

FIG. 7. Radiative temperature of hot-source T_{Rad}^{Hot} (first row) with absolute and relative uncertainties (second row) and difference input intensity ΔI (third row) for spectral ranges 0–850 GHz (left column) and 60–525 GHz (right column). (a) T_{Rad}^{Hot}. From 70–700 GHz T_{Rad}^{Hot} varies smoothly but is decreased by about 100 K with respect to its physical temperature 873 K. The characterization is corrupted at the water absorption lines around 556.94 GHz and 752.03 GHz. Below 70 GHz and above 700 GHz the poor SNR affects the characterization. (b) From 100 GHz onwards T_{Rad}^{Hot} decays from 800 K to 760 K at 500 GHz. (c) Uncertainties σ_{THot} (black) and $\sigma_{\Delta I}$ (dashed). Neglecting water absorption lines around 556.94 GHz and 752.03 GHz both uncertainties are small for a broad spectral range: 6 K at 100 GHz, 2 K at 300 GHz, and 3.5 K at 700 GHz. Below 70 GHz and above 700 GHz, the poor SNR increases the uncertainties. (d) Relative uncertainties $\sigma_{THot}/T_{Rad}^{Hot}$ (black) and $\sigma_{\Delta I}/\Delta I$ (dashed). Both ratios fall below the 1% level above 100 GHz. (e) ΔI on logarithmic scale. (f) ΔI on linear scale.

ΔI covers two orders of magnitude for the spectral range 60–725 GHz. Using Gaussian error propagation, the relative uncertainty $\sigma_{\Delta I}/\Delta I = \sqrt{\sigma_{TCold}^2 + \sigma_{THot}^2}/\left(T_{Rad}^{Hot} - 309.8\ \mathrm{K}\right)$ becomes available (see Figs. 7(c) and 7(d)). Compared with $\sigma_{THot}/T_{Rad}^{Hot}$ the ratio $\sigma_{\Delta I}/\Delta I$ is increased by a factor two but is still below 1% above 110 GHz. The absorption lines of water vapour at 556.94 GHz and 752.03 GHz substantially restrict the derivation of ΔI at these frequencies.

E. Grid transmission

The transmission of the attenuator grid inserted in the interferometer back end during plasma operation (see component 8 in Fig. 3) is determined by local measurements using two broadband sources. For practical reasons, the TK material at ambient temperature and liquid nitrogen temperature is chosen. The interferograms are acquired for both sources with the grid (G) and without the grid (NoG) in place. The ratio of the corresponding recovered difference spectra gives the grid transmission $T = \Delta S^{\mathrm{G}}/\Delta S^{\mathrm{NoG}}$. In the spectral range 70–700 GHz, the transmission oscillates in the range 0.31–0.35 (see Figs. 8(a) and 8(b)). By the uncertainty σ_T (see Fig. 8(c)) and the relative uncertainty σ_T/T (see Fig. 8(d)) T is identified with high reliability in the spectral range 70–725 GHz neglecting the interval around the water absorption line at 556.94 GHz.

F. Calibration factors

In general, Eq. (1) defines the calibration factors C_f using the recovered difference spectrum ΔS, the difference input intensity ΔI, and the grid transmission T (see Secs. IV B–IV E).

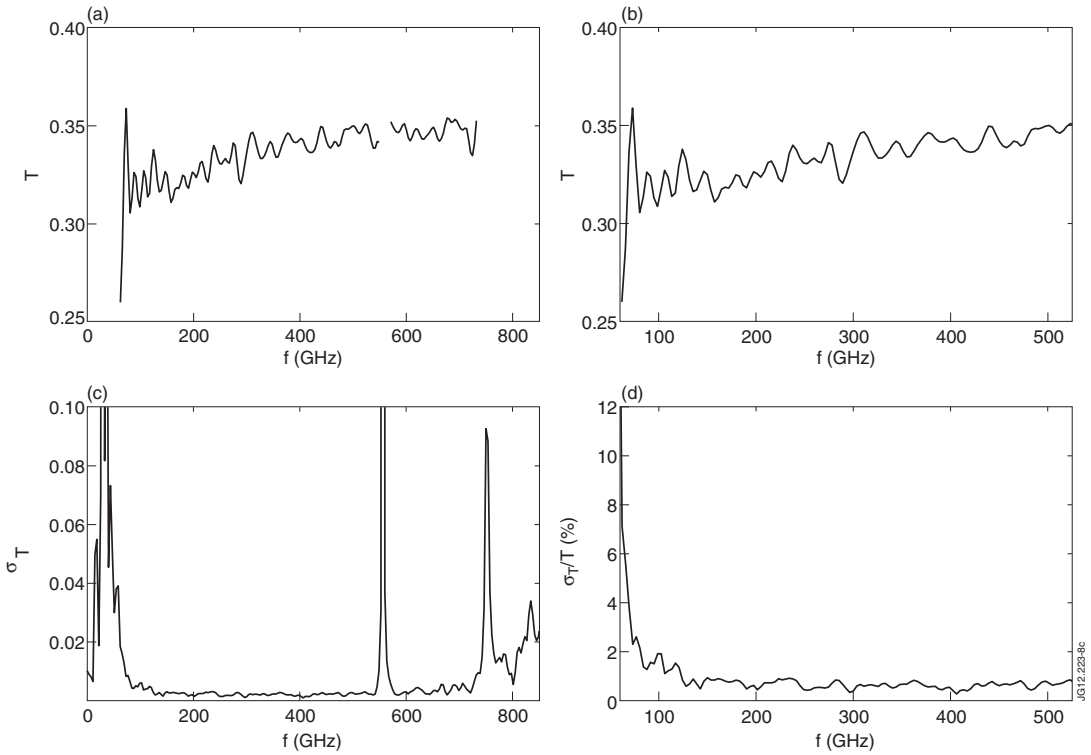

FIG. 8. Spectral characterization of grid transmission T. (a) T up to 850 GHz. T oscillates in the range 0.31–0.35 (~5 dB) for 70–700 GHz. (b) T for spectral range 60–525 GHz. (c) Uncertainty σ_T. T is determined with high precision from 70 to 700 GHz neglecting spectral ranges for water absorption lines. (d) Relative uncertainty σ_T/T for spectral range 60–525 GHz. Above 80 GHz σ_T/T falls below 2%. Below 70 GHz the characterization becomes unreliable.

In the following, the year of the derivation is used as upper index to distinguish different calibration factors sets. Since the relative uncertainty of C_f^{2010} evaluated by $\sigma_C/C_f^{2010} = \sqrt{(\sigma_{\Delta S}/\Delta S)^2 + (\sigma_{\Delta I}/\Delta I)^2 + (\sigma_T/T)^2}$ remains below 10% (see Fig. 9(c)), the spectral range 60–525 GHz is qualified to be presented (see Fig. 9(a)). Around 90 GHz C_f^{2010} has a maximum. Below 90 GHz the sensitivity reduces strongly by about one order of magnitude over 30 GHz as does the reliability. From 90 GHz to 525 GHz C_f^{2010} drops globally by more than one order of magnitude but shows locally minima and maxima pointing to resonances. The relative uncertainty is at the 1% level and increases from 350 GHz onwards.

Compared with the calibration factor set C_f^{1996} (see Fig. 9(a)), the spectral shape of C_f^{2010} is similar, especially for the second harmonic range 100–200 GHz which is the most important for the determination of the T_e profile at JET. However, on absolute scale the set C_f^{1996} exceeds C_f^{2010}. Thus, the diagnostic has become apparently less sensitive assuming that both sets have been determined correctly. This reduction can be found as well above 125 GHz for the set C_f^{2007} (Ref. 20, see Fig. 9(a)). The ratio C_f^{1996}/C_f^{2010}, expressing the relative change for each spectral channel, reveals a general increase of the detected intensity and thus the radiation temperature by about 15% in the spectral range 100–200 GHz (see Fig. 9(b)). For the third harmonic range, a stronger variation of C_f^{1996}/C_f^{2010} between 1.05 and 1.3 is present. Thus, the calibration in 2010 affects the spectral range of the 2nd and 3rd harmonic in different ways. The application of C_f^{2010} and C_f^{1996} to JET pulse data using Eq. (2) is shown in Fig. 9(d). Thereby, the intensity is presented in terms of radiation temperature T_e^{Rad}. The data chosen are recorded for a plasma with low magnetic field (pulse 79 777, t = 57.28 s, $B_{Vac} = 1.83$ T, $n_{e0} = 3\times10^{19}$ m^{-3}) and high magnetic field (pulse 79 759, t = 54.04 s, $B_{Vac} = 3.42$ T, $n_{e0} = 7\times10^{19}$ m^{-3}). For both cases, the ratio of the 2nd (at 100 GHz and 190 GHz) to the 3rd harmonic remains at the same level for the plasma centre. For the high field case, the wiggly structure is removed in the spectral range 275–350 GHz within the uncertainties by using C_f^{2010}. In addition, the 4th harmonic is available above 350 GHz. However, the high frequency range suffers from the influence of the water absorption lines.

G. Discussion

The difference between the two calibration sets, C_f^{1996} and C_f^{2010}, is about 15% on the absolute level showing a reduced sensitivity for the latter. Therefore, the application of the sets to the same uncalibrated plasma spectra results directly in an increase of the T_e values of that order. Unfortunately, the change in the sensitivity of the instrument cannot be resolved temporally, since no absolute calibration has been performed between 1996 and 2007. The latter delivered the calibration set C_f^{2007} (see Fig. 9(a)), which was also reduced with respect to C_f^{1996} above 125 GHz but in this case by approximately 25%.[20] However, it is likely that C_f^{2007} suffered from problems like uncertain placing of the calibration sources in front of the in-vessel antenna, insufficient integration time, and interferogram data superimposed with spurious signals as revealed by the approach for the session in 2010

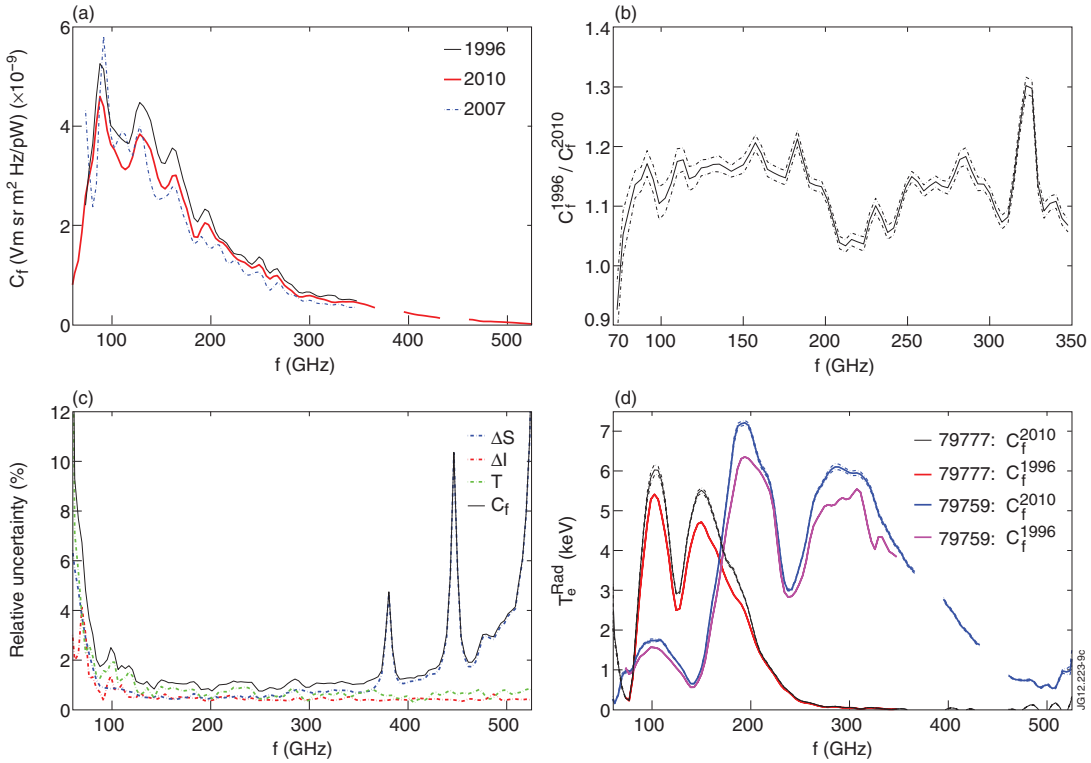

FIG. 9. Results of absolute calibration for JET Michelson interferometer carried out in 2010. (a) Absolute calibration factor sets C_f^{1996} (black), C_f^{2010} (red), and C_f^{2007} (dashed, blue) derived in 1996, 2010, and 2007, respectively. For the spectral range 73–347 GHz, C_f^{2010} and C_f^{1996} have a similar spectral shape but differ on absolute scale. Hence, the diagnostic has become less sensitive. The session in 2007 follows mainly the spectral trend. (b) Relative change expressed by ratio C_f^{1996}/C_f^{2010} (solid). In the spectral range used for plasma temperature measurements (100–200 GHz), the radiation temperature for C_f^{2010} is increased by about 15%. The uncertainty of C_f^{2010} (see (c)) translates into a narrow band (dashed). (c) Relative uncertainties for grid attenuation T (green, dashed), difference input intensity ΔI (red, dashed), recovered difference spectrum ΔS (blue, dashed), and calibration factors C_f^{2010} (black). The latter is evaluated by Gaussian error propagation. Below 100 GHz T and above 350 GHz ΔS drive the overall uncertainty. (d) Measured ECE spectra in terms of radiation temperature T_e^{Rad} using sets C_f^{2010} (black, blue) and C_f^{1996} (red, magenta). JET plasmas with low toroidal magnetic field (B = 1.83 T, $n_{e0} = 3\times10^{19}$ m^{-3}, t = 57.28 s, pulse 79 777) and high toroidal magnetic field (B = 3.42 T, $n_{e0} = 7\times10^{19}$ m^{-3}, t = 54.04 s, pulse 79 759) are chosen.

(see Fig. 5(a)). Nevertheless, an apparent considerable change in the system response as first indicated by the calibration measurements in 2007 has been confirmed by the calibration in 2010 although to a lesser extent. As a consequence, the data taken by the Michelson interferometer and the heterodyne radiometer have been reprocessed from the JET campaign C20, which started in 2008, using C_f^{2010}.

The determination of the spectral variation of C_f^{2010} is very precise in the main spectral range 100–350 GHz due to the low level of noise in the measurement (see Fig. 9(c)). However, the accuracy of the absolute level of C_f^{2010} could suffer from the influence of systematic errors. The potential causes of systematic errors are listed below and whenever possible an estimate of their magnitude and a strategy for a further investigation are given.

(i) Amplifier setting: The ratio C_f^{1996}/C_f^{2010} (see Fig. 9(a)), which is around 1.15 except for minor spectral regions, suggests that if a systematic error is the cause of the difference, then it must affect all spectral channels equally. Such an effect can be caused by the amplifier setting. Since the setting increment is constant at 2 dB (26%), a wrongly noted amplification seems unlikely.

(ii) Bias voltage: The detector sensitivity is dependent on its bias voltage V_{Bias} supplied by batteries. Local measurements show that the sensitivity has a maximum around $V_{Bias} = 7$ V for all spectral components. The corresponding increase in sensitivity is ~7% compared to $V_{Bias} = 10$ V which was used during the session in 2010. The decrease in the sensitivity by about 15% is possible if V_{Bias} is set to less than 4 V, which is eliminated for the calibration session in 2010. Furthermore, V_{Bias} needs to be held at the same level, which is 10 V, for plasma and calibration operation. Therefore, since 2011 V_{Bias} is monitored, and if mandatory the batteries are recharged.

(iii) Linearity of diagnostic sensitivity: The application of C_f^{2010} in Eq. (A2) to analyse plasma data is justified if the diagnostic response remains linear even for input signals which are some orders of magnitude larger than those during calibration. Subsequent to the calibration a full linearity check of the detector together with both amplifier stages has not been done. Nevertheless, the linearity was checked in 1984.[23] In addition, recent tests of a detector unit with attached first amplifier stage, which are both similar to the equipment used by the calibrated interferometer, and the second amplifier stage (see Sec. III C) confirm a linear response characteristics even after some decades of usage.

(iv) Separate daq systems for plasma and calibration operation: Measurements verify that a conversion factor

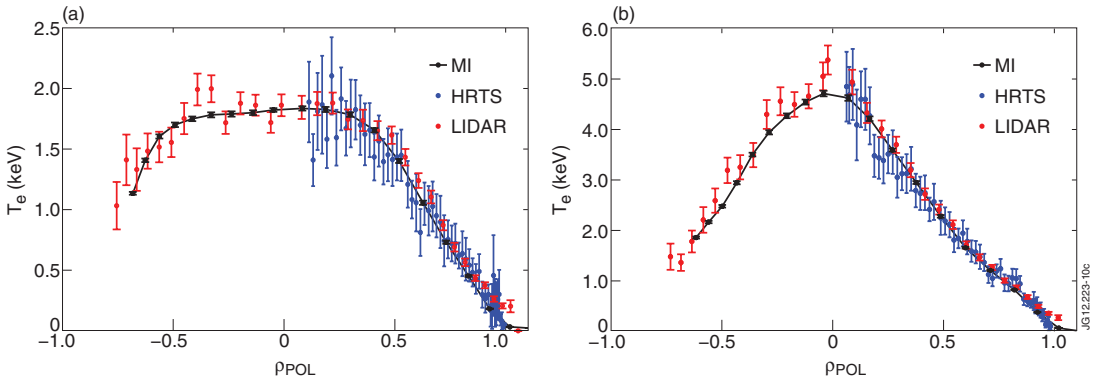

FIG. 10. Typical T_e profiles measured independently by ECE and TS diagnostics. The profile for the MI (black), the high-resolution Thomson scattering diagnostic (HRTS, blue), and the time-of-flight TS diagnostic (LIDAR, red) is mapped using equilibrium information provided by EFIT.[42] The uncertainties for the profile relying on the Michelson interferometer arise from the uncertainties of the calibration factors (see Fig. 9(c)). Thereby, the uncertainty in the absolute level is estimated to be ~5%. For HRTS and LIDAR, the uncertainties are purely statistical obtained from photon noise for the plasma measurement. Within the uncertainties the profiles are in good agreement. (a) JET pulse 83 200 at t = 51.87 s. (b) JET pulse 83 361 at t = 59.38 s.

between the two daq systems (see Sec. II D) exists. In the branch for the plasma daq system, a slight attenuation is present at the 2% level. Hence, strictly speaking, C_f^{2010} need to be decreased by that fraction. Instead of doing that, the calibration daq hardware is used for plasma operation from pulse 83 144 as well.

(v) Black body property of TK material: Below 100 GHz the TK material loses its black body property. Since it is expected that the absorption remains close to unity below the frequency 100 GHz, the effect on the spectral characterization of the hot-source and the calibration factors for the Michelson is estimated to be below the 5% level for the spectral range 60–100 GHz. However, since the determination of the T_e profile at JET relies mainly on the spectral range 100–200 GHz, the effect of this systematic error is of minor interest. Nevertheless, another type of the TK material[38] could possibly be used to cover the spectral range 50–100 GHz.

(vi) Spectral characterization of hot-source: As long as the antenna pattern is filled by the sources, which are placed at the distance of 15 cm to the antenna during the measurements in the diagnostic hall, and for the spectral range of interest the black body property of the TK material holds, the spectral characterization of the hot-source is valid. The former condition is presumed to be fulfilled, but if it is not, then, in principle, an under- or an overestimation of T_{Rad}^{Hot} by 10% is thinkable dependent on the radiation temperature of the lab and the actual shape of the local antenna pattern. As stated in (v) the characterization is systematically affected below 100 GHz, because of the changing properties of the TK material.

(vii) Filling in-vessel antenna pattern by hot-source: Simulations of the in-vessel antenna pattern for the spectral range 70–500 GHz and the modes TE10 and TE01 confirm that the hot-source is placed close enough at the distance 33 cm from the antenna. However, potentially this could be a source for a systematic error. Because of the TE10 mode filter (see Sec. II A) higher order modes should not play a major role, at least not at the level of 15%. The experimental investigation of the antenna pattern is planed during the JET shut-down phase starting in 2012. Ideally, the antenna pattern should be determined by a setup which is able to scan the two-dimensional plane perpendicular to the line of sight employing a monochromatic source. This would be difficult to do but scans of the distance between the hot-source and the antenna are foreseen.

Besides the possible systematic errors listed above the comparison of the electron temperature profile T_e measured independently by the Michelson interferometer (ECE diagnostic) and the TS diagnostics at JET gives confidence in the calibration made (see Figs. 10(a) and 10(b)). Thereby, for both TS diagnostics, which comprises the time-of-flight diagnostic LIDAR[8,9] and the high-resolution TS diagnostic HRTS,[10] the recent calibrations are used which were determined independently subsequent to refurbishments in 2010/2011.

V. CONCLUSIONS

Several aspects of the hardware, absolute calibration, and analysis techniques for the Michelson interferometer diagnostic at JET have been extensively described. The diagnostic benefits from a simple design and robust hardware components, especially for the back end, which makes faults unlikely. In case of a hardware fault, which is limited to components located in the diagnostic hall, the down-time is kept to a minimum. In addition, in-built protective measures reduce possible damage to the diagnostic. Therefore, during plasma operation maintenance work becomes minimal and the diagnostic has excellent reliability. The major operational task is the preparation and analysis for the absolute calibration using the hot/cold technique. The current implementation of the calibration procedure at JET, which employs the stand-alone setup and the specially developed digital averaging technique, demonstrates the derivation of the calibration factor set with high precision from high quality raw data. Since the in-vessel session data have been acquired on consecutive days and nights without malfunction of the equipment, the influence of changing ambient temperature along the transmission line is included. The setup parameters like the physical temperatures of the sources used have been monitored throughout the session. No abnormal behaviour was found.

For the spectral range 80–500 GHz, the calibration factor set is derived statistically with relative uncertainty below 5%.

Especially, for the spectral range 100–350 GHz, which is the most important for the JET plasma parameter range, the relative uncertainty is less than 2%. The most significant potential systematic error is probably the extent to which the in-vessel antenna pattern is filled with the hot-source. To investigate this further, during the next JET shut-down the distance between the electrically heated source and the antenna will be scanned. Thereby, an antenna extension will be employed to reduce the distance to less than 33 cm.

Below 100 GHz the TK material, which is essential for the calibration, starts to lose its property of being a good microwave absorber material.[38] Therefore, a systematic error is introduced whose effect has not been investigated so far.

Compared to the previous calibration factor set derived in 1996 the spectral shape is similar but on absolute scale the recent set shows that the sensitivity of the instrument has decreased by about 15%. Accordingly, for plasma operation the ECE spectrum and, therefore, the electron temperature increase. The exact cause of the reduction in sensitivity is not understood so far, but ageing of the detector element is a possibility.

Since the Michelson is the cornerstone of the ECE diagnostic system at JET, frequent application of the calibration procedure is recommended as carried out in the early years of operating the ECE diagnostic. This enables a future study of the sensitivity for several years as done in the timeframe 1984–1994. In addition, the monitoring of important parameters like the bias voltage supplying the detector is already on-going.

The calibration of the Michelson in 2010 led to a general improvement of the determination of the T_e profile at JET and agree well with the profiles measured independently by the TS diagnostics LIDAR and HRTS.

Besides its reliability the Michelson interferometer at JET demonstrates that continuous operation for days is achievable during calibration operation, and therefore it is applicable to the future tokamak ITER which has a pulse duration of less than 30 min. In addition, in principle, an interferometer enables the probing of the ECE spectrum even in the terahertz range. However, it is essential that frequent calibrations can be carried out, and to make these calibrations possible the calibration sources should be included in the system design. The calibration needs to be carried out up to 1 THz, at least. The Michelson at JET has shown by local measurements to be sufficiently sensitive to characterize the hot-source and the grid transmission up to the frequency 0.7 THz. By removing the filter inserted to limit the infrared spectrum to enter the cryogenic vessel, and improving the attenuation of the transmission line between the in-vessel antenna and the interferometer back end, it is believed that the sensitivity of Michelson would be suited for a successful absolute calibration up to 1 THz on ITER.

ACKNOWLEDGMENTS

The authors thank P. Trimble for technical support and P. Heesterman for developing the monitoring and steering software for the calibration session in 2010. The efforts of C. Hogben for the successful integration of the daq system used during the latest calibration to the JET environment for plasma operation are acknowledged. Due to the continuous interest of Dr. A. Costley, one of the designer of the Michelson interferometer at JET and ITER, many fruitful discussions have been carried out, and therefore he has earned special thanks. This work was supported by EURATOM and carried out within the framework of the European Fusion Development Agreement Tasks. The views and opinions expressed herein do not necessarily reflect those of the European Commission.

APPENDIX: GENERAL DERIVATION OF CALIBRATION FACTORS

The diagnostic of type Michelson interferometer translates the intensity spectrum at the input into the interferogram at the output according to the intrinsic sensitivity. The corresponding diagnostic model can be expressed by

$$V(x) = A\int I_\sigma C(\sigma)\cos(2\pi\sigma x)\,d\sigma + V_{BG}(x) = A\mathrm{FT}_{\cos}\{I_\sigma C\} + V_{BG} \tag{A1}$$

assuming that the post-detection amplifier with amplification A removes the dc part $\int I_\sigma C d\sigma$. The model links the interferogram V with the cosine transform $\mathrm{FT}_{\cos}$ of the product of the input intensity or spectral radiance I_σ and the diagnostic sensitivity C. To be clear, V with unit volt varies with the optical path difference x, I_σ with unit W/(m^2 sr m^{-1}) and C with unit m^2 sr V/W depend both on the inverse wavelength σ. Furthermore, the model (A1) comprises the background voltage signal V_{BG} which is present for an arbitrary input spectrum. For the Michelson interferometer at JET, V_{BG} is negligible when ECE spectra are probed emitted by plasmas with typical temperature well above 10 eV. Therefore, once the sensitivity C is specified via an absolute calibration, i.e., the experimental determination of C, the inversion delivers the ECE spectrum by

$$I_\sigma = A^{-1}\frac{\mathrm{FT}_{\cos}^{-1}\{V\}}{C} = \frac{S}{C} \tag{A2}$$

using the recovered spectrum S in the numerator. However, if the calibration technique like at JET relies on sources with temperatures below 1000 K (<0.1 eV), V_{BG} becomes important. The background is removed for using the hot/cold technique. Thereby, two different sources, a cold and a hot one with corresponding spectra $I_\sigma^{Cold/Hot}$, are placed in front of the diagnostic antenna. As a consequence, the difference interferogram

$$A^{-1}(V^{Hot} - V^{Cold}) = \mathrm{FT}_{\cos}\{(I_\sigma^{Hot} - I_\sigma^{Cold})C\} \tag{A3}$$

becomes proportional to the cosine transform of the product of the difference input intensity and the sensitivity. The inverse operation reveals the sensitivity

$$C = A^{-1}\frac{\mathrm{FT}_{\cos}^{-1}\{V^{Hot} - V^{Cold}\}}{I_\sigma^{Hot} - I_\sigma^{Cold}} = \frac{A^{-1}}{c}\frac{\mathrm{FT}_{\cos}^{-1}\{V^{Hot} - V^{Cold}\}}{I_f^{Hot} - I_f^{Cold}} = \frac{1}{c}\frac{\Delta S}{\Delta I} = \frac{C_f}{c} \tag{A4}$$

as the ratio of the recovered difference spectrum ΔS to the difference input intensity ΔI with unit W/(m^2 sr Hz) multiplied with the speed of light c. Alternative to C the quantity C_f with unit (Vm m^2 sr Hz/W) is introduced which plays a role for the Michelson interferometer at JET. Theoretically, the absolute calibration obtains the calibration function which represents the sensitivity for the spectral range with sufficient SNR. However, the previous derivation of the calibration function needs to be adapted to real world interferometers. In practice, the interferogram is sampled at a finite number of data points. Therefore, the continuous operation $\mathrm{FT}_{\cos}^{-1}$ is replaced by the discrete operation $\mathrm{DFT}_{\cos}^{-1}$. In addition, the information about the ZPD position at which the optical path difference vanishes is uncertain, and dispersion in the diagnostic might be present. Hence, phase correction (PC) needs to be applied to the recovered spectrum for which the operation $\mathrm{DFT}_{\sin}^{-1}$ is mandatory. Other common techniques or tricks are used: zero-padding to increase the frequency resolution and to meet the conditions for discrete fast Fourier transformation DFFT^{-1} routines; apodization of the interferogram data by window function g to reduce spectral leakage. Altogether the continuous calibration function is represented by a set of calibration factors calculated by

$$C_f = \frac{\Delta S}{\Delta I} = A^{-1}\frac{\mathrm{PC}\left(\mathrm{DFFT}^{-1}\left\{g\left(V^{Hot}-V^{Cold}\right)\right\}\right)}{\Delta I}. \quad \text{(A5)}$$

The calibration factors C_f become dependent on the specific implementation of how the difference interferogram is processed, but the impact is expected to be small. However, the implication is that the coherence between C_f and the recovered spectrum S calibrated in Eq. (A2) is only guaranteed when the interferogram V is processed like the difference interferogram in (A5).

[1] D. H. Martin and E. Puplett, Infrared Phys. **10**, 105 (1969).
[2] F. J. Stauffer, D. A. Boyd, R. C. Cutler, M. Diesso, M. P. McCarthy, J. Montague, and R. Rocco, Rev. Sci. Instrum. **59**, 2139 (1988).
[3] M. E. Austin, R. F. Ellis, J. L. Doane, and R. A. James, Rev. Sci. Instrum. **68**, 480 (1997).
[4] A. E. Costley, Fusion Sci. Technol. **55**, 1 (2009).
[5] A. E. Costley, E. A. M. Baker, M. G. Kiff, and G. F. Neill, in *Proceedings of the 3rd Joint Workshop on Electron Cyclotron Emission and Electron Cyclotron Resonance Heating, Madison, 1982* (University of Wisconsin, Madison, USA, 1982), p. 1.
[6] E. A. M. Baker, D. V. Bartlett, D. J. Campbell, A. E. Costley, M. G. Kiff, and G. F. Neill, in *Proceedings of the 8th International Conference on Infrared and Millimeter Waves, Miami, 1983*.
[7] A. E. Costley, E. A. M. Baker, D. V. Bartlett, D. J. Campbell, M. G. Kiff, S. E. Kissel, G. F. Neill, and P. F. Roach, in *Proceedings of the 5th Joint Workshop on Electron Cyclotron Emission and Electron Cyclotron Resonance Heating, San Diego, California, 1985* (G A Technologies Inc., San Diego, USA, 1985), p. 18.
[8] C. W. Gowers, B. W. Brown, H. Fajemirokun, P. Nielsen, Y. Nizienko, and B. Schunke, Rev. Sci. Instrum. **66**, 471 (1995).
[9] H. Salzmann, J. Bundgaard, A. Gadd, C. Gowers, K. B. Hansen, K. Hirsch, P. Nielsen, K. Reed, C. Schroedter, and K. Weisberg, Rev. Sci. Instrum. **59**, 1451 (1988).
[10] R. Pasqualotto, P. Nielsen, C. Gowers, M. Beurskens, M. Kempenaars, T. Carlstrom, D. Johnson, and JET-EFDA Contributors, Rev. Sci. Instrum. **75**, 3891 (2004).
[11] M. Bornatici, R. Cano, O. De Barbieri, and F. Engelmann, Nucl. Fusion **23**, 1153 (1983).
[12] E. de la Luna, J. Sánchez, V. Tribaldos, JET-EFDA Contributors, G. Conway, W. Suttrop, J. Fessey, R. Prentice, C. Gowers, and J. M. Chareau, Rev. Sci. Instrum. **75**, 3831 (2004).
[13] M. Zerbini, J. M. Chareau, D. Mazon, M. Riva, R. Felton, E. Joffrin, M. Lennholm, and R. Prentice, in *Proceedings of the 12th Joint Workshop on Electron Cyclotron Emission and Electron Cyclotron Resonance Heating, Aix-en-Provence, France, 2002*, edited by Gerardo Giruzzi (Association Euratom-CEA sur la Fusion, France), p. 227.
[14] L. Barrera, E. de la Luna, L. Figini, M. N. A. Beurskens, M. Brix, F. Castejón, P. C. de Vries, D. Farina, M. Kempenaars, P. Lomas, J. Mailloux, I. Nunes, E. R. Solano, and JET-EFDA Contributors, Plasma Phys. Controlled Fusion **52**, 085010 (2010).
[15] A. Simonetto, C. Sozzi, S. Garavaglia, J. A. Fessey, S. Nowak, and JET-EFDA Contributors, Rev. Sci. Instrum. **82**, 113506 (2011).
[16] P. Buratti and M. Zerbini, Rev. Sci. Instrum. **66**, 4208 (1995).
[17] S. Schmuck, J. Svensson, E. de la Luna, L. Figini, T. Johnson, B. Alper, M. Beurskens, J. Fessey, T. Gerbaud, A. Sirinelli, and JET EFDA Contributors, in *Proceedings of the 38th EPS Conference on Plasma Physics, Strasbourg, France, 2011*, edited by A. Becoulet, T. Hoang, U. Stroth, O. Scholten, and P. Helfenstein (European Physical Society, 2011), p. 1512.
[18] D. Farina, L. Figini, P. Platania, and C. Sozzi, in *Proceedings of Burning Plasma Diagnostics: An International Conference, Varenna, Italy, 2007*, edited by G.Gorini, F. P. Orsitto, E. Sindoni, and M. Tardocchi (American Institute of Physics, 2007), p. 128.
[19] J. Svensson, A. Werner, and JET EFDA Contributors, in *Proceedings of the 2007 IEEE International Symposium on Intelligent Signal Processing (WISP 2007), Alcala de Henares, Spain, 2007* (IEEE, 2007), p. 1.
[20] M. Zerbini, "In-Vessel Calibration 2007," Internal JET Report, 2007.
[21] A. E. Costley, E. A. M. Baker, D. V. Bartlett, D. J. Campbell, M. G. Kiff, and G. F. Neill, in *Proceedings of the 4th Joint Workshop on Electron Cyclotron Emission and Electron Cyclotron Resonance Heating, Rome, Italy, 1984* (ENEA, 1984), p. 1.
[22] E. A. M. Baker, D. V. Bartlett, D. J. Campbell, A. E. Costley, D. J. Daly, A. Dellis, L. C. J. M. De Kock, and J. Fessey, in *Proceedings of the 4th Joint Workshop on Electron Cyclotron Emission and Electron Cyclotron Resonance Heating, Rome, Italy, 1984* (ENEA, 1984), p. 11.
[23] E. A. M. Baker, D. V. Bartlett, D. J. Campbell, A. E. Costley, A. E. Hubbard, and D. G. Moss, in *Proceedings of the 4th Joint Workshop on Electron Cyclotron Emission and Electron Cyclotron Resonance Heating, Rome, Italy, 1984* (ENEA, 1984), p. 23.
[24] D. V. Bartlett, D. J. Campbell, A. E. Costley, S. Kissel, N. L. Cardozo, C. W. Gowers, S. Nowak, T. Oyevaar, N. A. Salmon, and B. J. Tubbing, in *Proceedings of the 6th Joint Workshop on Electron Cyclotron Emission and Electron Cyclotron Resonance Heating, Oxford, UK, 1987* (UKAEA Culham Laboratory, 1987), p. 137.
[25] Specification of Cryogenic Vessel and Detectors, QMC Instruments Ltd., 1985.
[26] F. D. Robinson, "Performance of indium antimonide as a far infra-red detector from 0.4–30 K," M.Sc. Astrophysics, Queen Mary College, 1979.
[27] H. Ooesterbeek and M. Zerbini, "Diagnostic schematic diagram," *JET Data Handbook KK1* (2006).
[28] H. Ooesterbeek and M. Zerbini, "Basic information for JET Michelson interferometer," *JET Data Handbook KK1* (2006).
[29] D. V. Bartlett, C. Bishop, R. Cahill, A. McLachlan, L. Porte, and A. Rookes, in *Proceedings of the 9th Joint Workshop on Electron Cyclotron Emission and Electron Cyclotron Resonance Heating, Borrego Springs, 1995* (World Scientific Publishing C. Pte. Ltd, 1995), p. 485.
[30] 2012 © United Kingdom Atomic Energy Authority to use the image contact Graphics@ccfe.ac.uk.
[31] Emerson & Cuming Microwave Products, see http://www.eccosorb.eu/sites/default/files/techbulletins/eb010_eccosorb_an.pdf.
[32] Thomas Keating Ltd., see http://www.terahertz.co.uk/index.php?option=com_content&view=article&id=150:TPXmaterial&catid=39:tkinstruments&Itemid=453.
[33] W. T. Welford and R. Winston, *The Optics of Nonimaging Concentrators* (Academic, New York, 1978).
[34] Incremental linear encoder model LIDA 190, Dr. Johannes Heidenhain GmbH.
[35] National Instruments, NI-PCI 6220, see http://sine.ni.com/nips/cds/view/p/lang/de/nid/14130.
[36] H. Bindslev and D. V. Bartlett, in *Proceedings of the 6th Joint Workshop on Electron Cyclotron Emission and Electron Cyclotron Resonance Heating, Oxford, UK, 1987* (UKAEA Culham Laboratory, 1987), p. 309.

[37]A. Loving, P. Allan, N. Sykes, S. Collins, and P. Murcutt, in *Proceedings of the 10th International Symposium on Fusion Nuclear Technology, Portland, 2011*.
[38]Tesselating Terahertz RAM radar absorbing material by Thomas Keating Ltd. See http://www.terahertz.co.uk for description and specifications.
[39]D. V. Bartlett, M. Zerbini, P. Blanchard and J. Fessey, *JET Data Handbook for Michelson Interferometer* (1988–2009).
[40]M. Zerbini, C. Sozzi, and A. Simonetto, in *Proceedings of the 15th Joint Workshop on Electron Cyclotron Emission and Electron Cyclotron Resonance Heating, Yosemite National Park, California, 2008*, edited by John Lohr (General Atomics, Inc., 2008), p. 227.
[41]C. D. Porter and D. B. Tanner, Int. J. Infrared Millim. Waves **4**, 273 (1983).
[42]L. L. Lao, J. R. Ferron, R. J. Groebner, W. Howl, H. S. John, E. J. Strait, and T. S. Taylor, Nucl. Fusion **30**, 1035 (1990).